〈일반논문〉
Journal of the Korean Society of Visualization, Vol. 14, No. 2 (31~39), 2016
(Manuscript received : 2016.07.27/Revised : 2016.08.19/Accepted : 2016.08.19)
DOI:http://dx.doi.org/10.5407/JKSV.2016.14.2.031

ISSN 1598-8430 Print
ISSN 2093-808X Online

Tomographic PIV measurement of internal complex flow of an evaporating droplet with non-uniformly receding contact lines

Hyoungsoo Kim† · Naser Belmiloud* · Paul W. Mertens**

Abstract We investigate an internal flow pattern of an evaporating droplet where the contact line non-uniformly recedes. By using tomographic Particle Image Velocimetry, we observe a three-dimensional azimuthal vortex pair that is maintained until the droplet is completely dried. The non-uniformly receding contact line motion breaks the flow symmetry. Finally, a simplified scaling model presents that the mechanical stress along the contact line is proportional to the vorticity magnitude, which is validated by the experimental results.

Key Words : Tomographic PIV, Evaporating droplet, Azimuthal vortex flow, Non-uniformly receding contact line

1. Introduction

When a sessile droplet evaporates, the contact line, the region where gas, liquid, and solid phases meet together, normally either pins or recedes. If the contact line pins to the substrate during evaporation, the wetting area is kept constant and the contact angle decreases with time until the droplet dried out.[1] Then, non-uniform evaporating flux induces a radial outward flow that transports particles towards the pinned contact line, and the particles are accumulated.[2-5] This phenomenon is the so-called coffee ring stain.[2] On the other hand, if a droplet is placed on a perfectly smooth and wetting surface, the contact line consistently recedes and the surface of the wetting area linearly decreases with time during evaporation.[6] In this case, not like the pinned example, an inward axisymmetric radial flow pattern is observed, i.e. flowing from the moving contact line to the center of the droplet.[7, 8] In sum, the internal flow pattern is related to the contact line receding pattern.

Besides, stick-and-slip contact line motion is also reported.[9-12] This non-uniformly receding contact line pattern is due to various reasons, e.g. heterogeneities of the surface, impurities inside the droplet, and so on. Orejon et al.[12] presented that the repetitive pinning and non-pinning motion is dependent on the colloids concentration in the vicinity of the contact line. However, for the stick-and-slip contact line motion of evaporating droplet, the quantitative flow field measurement is still lacking, which we aim to achieve in this work. We investigate the relationship between the local contact line motion (i.e., relative displacement) and the internal flow pattern.

† Department of Mechanical and Aerospace Engineering, Princeton University, Princeton, NJ 08544, USA
E-mail: hskim@princeton.edu
* SCREEN SPE Germany GmbH, Fraunhofer Strasse 7, 85737 Ismaning, Germany
** IMEC, vzw Kapeldreef 75, Heverlee 3001, Belgium

To date, the measurement of a flow pattern inside an evaporating droplet is usually done by conventional planar Particle Image Velocimetry (PIV).[2, 4] In the experimental aspect, we have to note here that the difficulties encountered in light distortion at the liquid-air interface. At the free interface, the measurement results are distorted by the refractive index jump. Kang et al.[13] tried to measure the lateral fluid motion of an evaporating droplet through the liquid-air interface by a direct ray tracing method. It is still challenging work to measure a flow field directly through the liquid-gas interface. In other ways, to minimize the optical distortion through the media, an inverted measurement system is commonly used[14, 15]. Pradhan and Panigrahi[14] performed the flow field measurement inside the evaporating droplet by using scanning confocal microscope. Kim et al.[15] obtained the full three-dimensional three velocity vector components (3D-3C velocity vectors) near the liquid-air interface by tomographic PIV with an inverted measurement system. Furthermore, they obtained the three-dimensional dewetting corner structure by using a tomographic reconstruction technique.[15] They showed that tomographic PIV is capable of measuring the complex micro-scale flow patterns where the liquid-air interface exists.

In this paper, we investigate a flow pattern of evaporating droplet where the contact line non-uniformly recedes in time and space. The three-dimensional flow field is explored by using tomographic PIV. Based on the result, we examine the relationship between the contact line receding pattern and internal flow field.

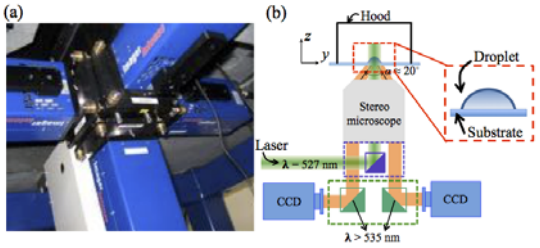

Figure 1. Tomographic PIV system: (a) Illustration of the PIV setup, with four PIV cameras mounted on a custom-made microscope at the bottom of the substrate. (b) Cross-sectional schematic of tomographic PIV system. Rhodamine-B fluorescent particles inside the droplet are volumetrically illuminated at 527 nm wavelength. The optical filters installed in front of each CCD camera only transmit light with wavelengths longer than 535 nm. The optical paths of four cameras go through a single microscope objective. The angle between the offset optical axes of the cameras is about $\alpha \approx 20^{\circ}$. The hood covers the measurement area to isolate from an environment.

2. Experiments

2.1 Substrate preparation

We use self-assembled monolayers (SAMs) in an organic solvent to design transparent substrates with different contact angles on-demand.[16, 17] The molecular self-assembly is mainly promoted by the dominant Van der Waals interaction between the lateral alkyl chains of the SAMs precursors.[18-20] However, the mechanism and kinetics of the self-organization phenomenon are still under investigation.

Nevertheless, according to one of the most accredited hypotheses, SAMs are created by the formation of a siloxane bond between the Si of the silane molecules and the oxygen of the hydroxyl groups on the glass substrate. It is then followed by a slow two-dimensional self-organization of the lateral chains. Initially, the adsorbate molecules form a nematic phase. Then, over a period of hours, it forms crystalline structures on the substrate surface. Areas of close-packed molecules nucleate and grow until the surface of a substrate is covered by a single

monolayer. The covalent bonds formed during silanization have higher energy and stability with respect to physisorbed films.[21] Furthermore, for dense SAMs, there is no leaching of water inside the substrate (i.e., impermeability of the substrate) and no chemical reaction between substrate and the colloidal solution (i.e., no change of the contact angle or roughness of the substrate).

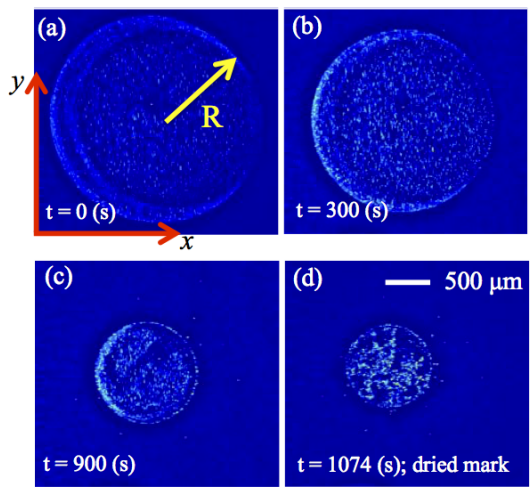

Figure 2. Evolution of evaporating droplet in time; (a) t = 0 (s), (b) t = 300 (s), (c) t = 900 (s), and (d) t = 1074 (s). The PIV images are captured where R is a initial radius of a droplet.

In this study, SAMs derived from 11-cyanoundecyltri-chlorosilane ($C_{12}H_{22}Cl_3NSi$) are deposited on 3×3 cm^2 glass substrates pre-cleaned by 15 min exposure to UV-ozone treatment in a Jelight UVO cleaner. The cleaned glass substrates are immersed for 30 min in a 5×10^{-3} M solution of 11-cyanoundecyltri-chlorosilane using toluene as a solvent. The resulting SAM is rinsed with toluene, ethanol, and deionized water and finally dried with nitrogen flow. The substrate surface presents cyano groups terminations which are chemically inert with respect to water and colloids (i.e., here, fluorescent particles for the PIV).

The measured water contact angle on the SAMs substrate is 50 ± 3° according to a standard side-view shadowgraphy measurement. In this experiment, the initial volume of the sessile droplet is 1.5 μl. The initial wetting area has a diameter of 2.6 mm. The droplet height is 0.6 mm at the center. The substrate sample is stored under ultra-clean dry-nitrogen ambient before experiments.

2.2 Tomographic PIV

A schematic of the experimental setup is presented in figure 1. To observe the flow field inside a droplet, the entire droplet needs to be accessed without minimal optical distortion for instance caused by reflection or refraction at the liquid-air interface. Therefore, the measurement system is mounted on an inverted custom-made microscope (see figure 1). To measure the fluid motion inside the evaporating droplet, we perform tomographic PIV that allows the measurement of 3D-3C velocity vectors in a volume. Furthermore, this method is able to reconstruct the liquid-air interface by an average-reconstructed intensity distribution.[15] For multi-camera measurement technique, an inverted (i.e., upside-down) custom-made microscope (Carl Zeiss Neolumar S1.5×) is equipped with optical filters set and with four dual-frame CCD cameras (LaVision Imager intense, 1376 × 1040 pixels, 12-bit dynamic range) is used for imaging, as shown in figure 1.

For the measurement of the volumetric flow field inside the droplet, the distilled water is seeded with 1.0 μm hydrophilic tracer particles (Duke Scientific Corp.) that are composed of polystyrene and fluorescent (Rhodamine-B). The particle volume fraction is 1.0 % in aqueous suspension of 1 μl and then the particles are diluted in 30 ml distilled water, so that the final particle volume fraction is approximately 3.3×10^{-5} %. In this experiment, the Stokes number, defined as $St = \tau_p/\tau_f$, where τ_p is the particle response time and τ_f is the time scale of fluid motion, is of the order of 10^{-9} because τ_p

($=1/18\rho_p d_p^2/\mu$) ~ 10^{-7} (s) and τ_f ($=R_{max}/U$) ~ 10^2 (s), where ρ_p is the density of the particle (1050 kg/m^3 for polystyrene), d_p the diameter of the particle (1 μm), R_{max} the initial droplet radius (1.3 mm), and μ the dynamic viscosity (10^{-3} Pa·s) of water. U is the mean flow speed, O(10 μm/s) that is obtained from the tomographic PIV. Furthermore, partides sedimentation effect due to the particle density is almost negligible because the sedimentation particle speed U_s ($= g(\rho_p - \rho)d_p^2/(18\mu)$) is much smaller than the flow speed, i.e. $U_s/U \sim 10^{-3}$. Therefore, the particles well follow the flow. We empirically obtain a particle concentration to prevent serious particle aggregation at the contact line (see figure 2 (a-c)).

A frequency-doubled Nd:YLF laser (Pegasus Laser 10 mJ, 527 nm) is used as a light source, which illuminates the entire droplet. The frequency of the flashing laser is 1 Hz to obtain the sequence PIV images and the laser exposure time is very short, e.g.

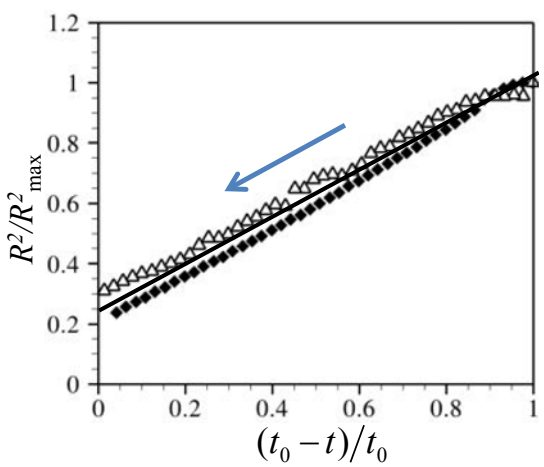

Figure 3. Evolution of droplet wetting areas, $R^2 \propto (t_0 - t)$ where x- and y- axes are normalized by t_0 and R_{max}^2, respectively. The solid diamond symbol is a current result case as shown in figure 2. t_0 is the time at which the droplet vanishes and R_{max} is an initial droplet radius. We also plot another non-uniformly receding droplet case which is an open triangular symbol. The solid line represents a linear fit to the results.

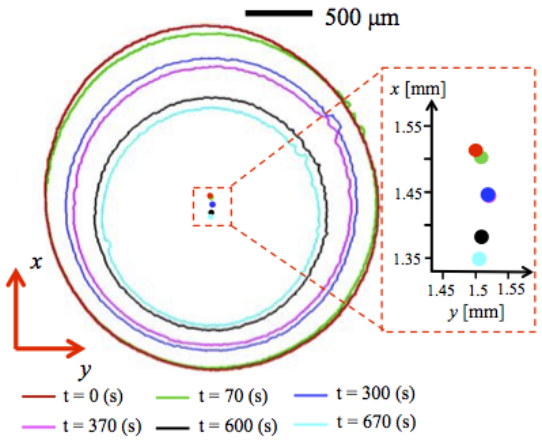

Figure 4. Contact line contours at different times. The line and circle colors indicate a different time, i.e. the red is at t = 0 (s), the green; t =70 (s), the blue; t = 300 (s), the magenta; t = 370 (s), the black; t = 600 (s), and the cyan; t =670 (s) (see the legend at the bottom of figure 4), which is extracted from the tomographic reconstruction results. In the red-dashed box, the center locations of contours are plotted where the color indicates the specific time as used in figure 4.

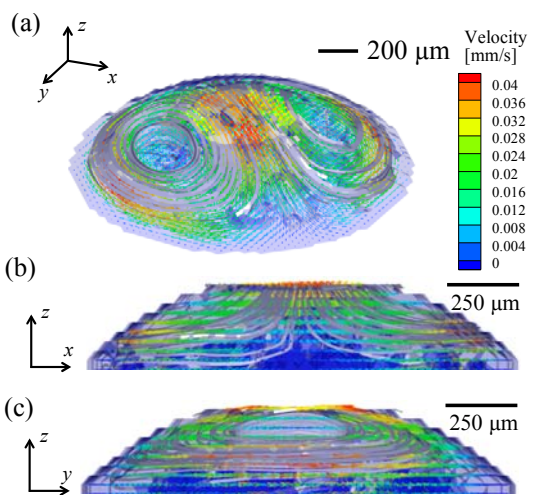

Figure 5. Tomographic PIV results: (a) Full 3D flow pattern inside evaporating droplet at t = 760 (s). Lateral views in (b) x-z plane and (c) y-z plane. Streamlines (white solid-bold lines) and velocity vectors (colors) in Cartesian coordinates where the colors represent the velocity magnitude. The bluish contour shell indicates the liquid-air interface, which is reconstructed by tomography.

shorter than $O(1\ \mu s)$. In this experiment, we assume that there is no laser heating effect (see Section 3). The camera frames and the lasers are synchronized using a commercial LaVision Programmable Timing Unit (PTU).

The experiment has always been carried out at relative humidity and temperature fixed to 40 % and 295 K, respectively. Those are controlled by an air-conditioning system of the confined lab. It is measured by a hygro-thermometer during experiments. To protect the droplet from environmental effects, we install a hood on top of the droplet and substrate.

A droplet is volumetrically illuminated and then all particles in the volume are scattered. Therefore, it is required to perform a proper image processing to minimize the background noise. First, a min-max filter is applied to normalize the image contrast.[22] Then, we used a sliding minimum filter to subtract background illumination and a 3 × 3 Gaussian smooth to reduce image noises on the particles. We perform a 3D calibration with volume self-calibration,[23] which reduces the calibration errors to 0.077 pixels corresponding to about 0.3 μm. The particle image displacement within a chosen interrogation volume (16 × 16 × 16 voxels) with 50 % overlap is obtained by the 3D cross-correlation of the reconstructed particle distribution at the two exposures. The whole pre- and post-processing and calibration procedure are performed by a commercial software (Davis 8.08, LaVision GmbH). The PIV experimental details are described in preceding works.[15]

3. Results and discussion

The drying water droplet with an initial (t = 0) volume of 1.5 μL is investigated where the contact line non-uniformly recedes. To completely dry this droplet, it takes about 1000 (s). Water has dynamic viscosity $\mu = 10^{-3}$ Pa·s, surface tension $\gamma = 0.072$ N·m^{-1}, and density $\rho = 998$ kg·m^{-3}. In this case, the droplet radius is smaller than a capillary length, i.e. $\kappa^{-1} = (\gamma/\rho g)^{1/2} > R$ where g is gravitational acceleration 9.8 m/s^2, and therefore gravity effect is negligible. Furthermore, the Bond number is smaller than unity, i.e. $\mathrm{Bo} = (\rho g R^2)/\gamma < 1$. The Reynolds number is much smaller than unity, $\mathrm{Re} = \rho UR/\mu \ll 1$ where the averaged flow velocity obtained from the tomographic PIV is $U = 10$ μm/s and the nominal droplet radius $R = 1.3$ mm. The surface tension is predominant compared to the inertia and the viscous forces where the Weber and capillary numbers are much smaller than unity, i.e. $\mathrm{We} = (\rho U^2 R)/\gamma \ll 1$ and $\mathrm{Ca} = \mu U/\gamma \ll 1$.

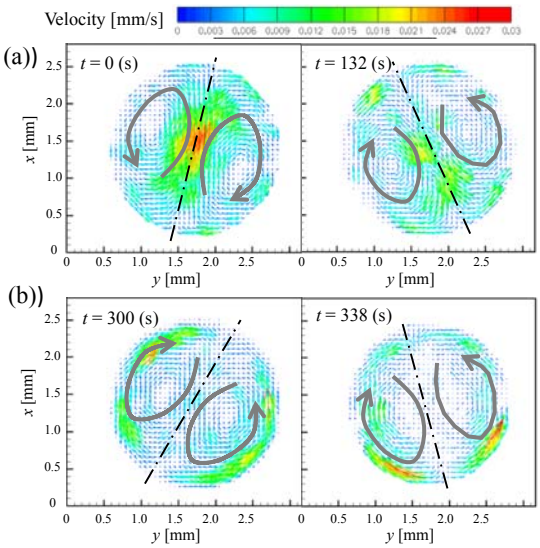

Figure 6. Tomographic PIV results close to the substrate (i.e., $z = 52$ μm). (a) Non-uniformly receding contact line regime at $t = 0$ and 132 (s). (b) Uniformly receding contact line regime at $t = 300$ and 338 (s). The dashed-dot line represents the axis of symmetric flow patterns. The vector color indicates the magnitude of the velocity vector.

During evaporation, the droplet wetting area linearly decreases with time as shown in figure 3, i.e. $R \propto (t_0 - t)^{1/2}$, where the area is obtained from measurement images. Therefore, the current evaporation is purely diffusive, i.e. no external

convection effect.[24] It means the water molecules diffuse through the liquid-air interface during evaporation. Practically, the convective evaporation effect was observed in a nano-scale droplet[25] and volatile liquid droplets.[26]

To investigate contact line movements, we extract the contact line contours from the reconstructed tomographic images. Figure 4 shows that the contact line non-uniformly recedes in time. For instance, during t = 0 ~ 70 (s), as shown in figure 4, the top part of the contact line recedes in time while the other side of the contact line is locally pinned. Then, the droplet center position is moved to the downward during this period (see the red-dashed box of figure 4). Namely, the contact line does not uniformly recede. In the next period (300 (s) ≤ t ≤ 370 (s)) the droplet center is almost stationary (see the blue and purple circles in the red-dashed box of figure 4). After then, the droplet non-uniformly recedes again during t = 600 ~ 670 (s).

The main reason of non-uniform contact line receding behaviors can be due to either small trace amounts of residues on the surface (i.e., heterogeneities) or temporarily accumulated particles in the vicinity of a contact line.[9-12] Additionally, we can also suspect that the SAM substrate in air may result in a random adsorption of Airborne Molecular Contamination (AMC).[27] During the experiment, the substrate is exposed to air. Then, the substrate condition can be locally changed. We presume that these effects cause the non-uniform receding contact line motion.

Additionally, in the current study, we assume that there is no significant thermal Marangoni effect along the liquid-air interface. The reasons are that firstly we kept the constant temperature and humidity in the hood and secondly it is reported that normally in the water droplet case the thermal Marangoni effect is very weak although Marangoni number is large.[28]

By tomographic PIV, we obtain the 3D-3C velocity flow field inside an evaporating droplet where the contact line non-uniformly recedes, as shown in figure 5. This is an instantaneous result at t = 760 (s) after depositing a sessile drop on a substrate. The result shows one pair of symmetric 3D vortices inside the evaporating sessile water droplet, as shown in figure 5 (b,c). The flow pattern is not axi-symmetric. In this measurement, the divergence RMS error ($\sigma_{\Delta x}$) [22] is 0.12 pixels, which is less than 1 μm in the actual system. Furthermore, the total net flow (ΔV) of measurement results is 7.7×10^{-9} m^3/s. This RMS error and the mass conservation error are consistent with a typical the measurement uncertainty reported for tomographic PIV.[15, 29]

Tomographic PIV is used to obtain the three-dimensional internal flow field and then in-plane flow patterns near the solid substrate (at z = 52 μm) is extracted from the three-dimensional results, which are presented in figure 6. The dashed-dot-line represents a symmetric axis of a vortex pair. Figure 6 (a) shows the flow pattern examples where the contact line does not uniformly recede. A shrinking rate of the receding contact line is continuously varied and then a tangential stress along near the liquid-air interface is no longer free. Presumably, this relative contact line movement causes to break the axi-symmetric flow pattern and creates the azimuthal vortex pair pattern.

In a different problem, a similar azimuthal vortex flow pattern was observed. Mampallil et al.[30] presented that electrowetting droplets can be partially pinned by using inhomogeneous substrates. Normally, AC electrowetting-induced flow in a droplet presents an axi-symmetric circulation flow pattern around the electrode due to thermal effects.[31] However, they reported when the contact line of the droplet is locally pinned by the patch and the other side freely recedes, a pair of azimuthal vortices is observed.

To further investigate the effect of the contact line movement on the internal flow pattern, we explore the evolution of a maximum vorticity inside evaporating droplet. Figure 7 shows that the vorticity

magnitude is associated with the receding pattern of the contact line. In I, III, and V regimes, the contact line receding pattern is non-uniform and then the vorticity magnitude increases. On the other hand, in II and IV regimes, contact lines almost uniformly recede everywhere (see the blue and magenta lines [or center positions] of figure 4) and the vorticity magnitude decreases in that period. This process repeats during the evaporation. As a consequence, the internal flow is related to dynamics of receding contact lines.

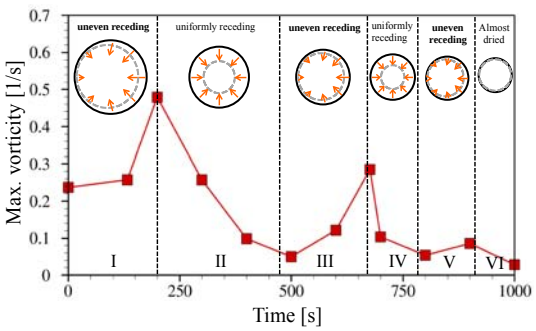

Figure 7. Evolution of the vorticity magnitude during droplet evaporation. I, III, and V are the case of non-uniformly receding contact lines. II and IV are almost uniformly receding cases. VI is an almost dried case. Insets describe a schematic of contact line dynamics transition.

In order to understand this, let us consider the force balance on a droplet volume element V enclosing the droplet interface S defined by the contour C:

$$\int_V \rho \frac{D\mathbf{u}}{Dt} dV = \int_S \boldsymbol{T} dS + \int_C \gamma \mathbf{s} d\ell, \quad (1)$$

where D/Dt is the matertial derivatives, $\mathbf{u}$ is a fluid velocity vector, and $\mathbf{s}$ the unit vector normal to contour C but tangent to interface S. $\boldsymbol{T}$ is the stress vector acting on the liquid interface. ℓ#is the arc length along the contact line and so $d\ell$ is a length increment along the curve C. The stress $\boldsymbol{T}$ is determined by the liquid phase because the hydrodynamic force exerted by air is negligible. It can be expressed in terms of the local fluid pressure and velocity field, $\boldsymbol{T} = -p\boldsymbol{I} + \mu\nabla(\mathbf{u} + [\mathbf{u}]^t)$ where $\boldsymbol{I}$ is a unit matrix and the superscript t denotes the transpose. Based on the scaling analysis (Re $\ll$ 1), the inertial force associated with acceleration within V is ignored. Furthermore, by using the Stokes theorem, we can obtain the stress balance on the droplet surface :

$$-p\mathbf{I} + \mu\nabla(\mathbf{u} + [\mathbf{u}]^t) = \nabla\gamma - \gamma\mathbf{n}(\nabla \cdot \mathbf{n}), \quad (2)$$

where $\mathbf{n}$ is a normal unit vector. Normally, in the evaporating droplet problem where the contact line is pinned everywhere, a zero shear stress boundary condition is applied at the liquid interface.[7, 32] However, in this study case, the tangential stress along near the liquid interface is no longer free because the shrinking rate of the droplet interface is not uniform everywhere while the contact line non-uniformly recedes.

On the right hand side of equation (2), the normal component term is described as the capillary pressure, which is constant everywhere. The tangential component of surface tension is mainly balanced with the viscous effect on the left hand side of equation (2). From this, we can describe the relationship that the vorticity magnitude is proportional to the surface tension gradient on the liquid interface:

$$\nabla\gamma \sim \mu\frac{U}{R} \approx \mu\omega, \quad (3)$$

where ~ means "of the order of", R is a radius of the droplet, and ω is a vorticity. As the tangential stress increases, the internal vortex flow is getting stronger as shown in figure 7. On the other hand, if the non-uniform receding contact line pattern is temporarily getting weaker, the vortex flow is feebly preserved and then the vorticity decreases, as shown in II and IV periods of figure 7.

4. Conclusion

In this paper, we investigated the internal flow pattern of an evaporating droplet where the contact line non-uniformly recedes and observed a pair of azimuthal vorticies, which is obtained by tomographic PIV. The non-uniform receding motion of the contact line induces stresses along the liquid-air interface that causes a peculiar azimuthal symmetric vortex flow pattern. By scaling analysis, we present that the vorticity evolution is related to the contact line receding trend, which is validated by experimental results. We believe that the tomographic PIV is a promising measurement technique that can obtain the flow pattern close to a liquid-air interface. Furthermore, we believe that this study is relevant to applications such as manipulation of the internal flow pattern of the droplet evaporation and control of the particle deposition pattern based on understanding of the flow pattern.

Acknowledgments

The research leading to these results has received funding from the European Community's Seventh Framework Programme (FP7/2007-2013) under grant agreement No. 215723. We thank Silvia Armini and Tinne Delande from IMEC for the preparation of the SAMs samples. Additionally, we acknowledge very useful conversation with B. Wieneke and S. Tokgoez from LaVision GmbH on tomographic PIV, the support of ASML Netherlands B.V. in funding the PIV set-up and of M. Riepen from ASML. Furthermore, we thank to S. Wilson, A. Darhuber, O. Shardt, and H. Masoud for valuable discussions to improve the paper.

REFERENCES

1) Y. O. Popov, *Physical Review E* 71, 036313 (2005).

2) R. D. Deegan, O. Bakajin, T. F. Dupont, G. Huber, S. R. Nagel, and T. A. Witten, *Nature* 389, 827 (1997).

3) R. D. Deegan, O. Bakajin, T. F. Dupont, G. Huber, S. R. Nagel, and T. A. Witten, *Physical Review E* 62, 756 (2000).

4) A´. G. Mar´ın, H. Gelderblom, D. Lohse, and J. H. Snoeijer, *Physical Review Letters* 107, 085502 (2011).

5) P. J. Yunker, T. Still, M. A. Lohr, and A. Yodh, *Nature* 476, 308 (2011).

6) H. Y. Erbil, G. McHale, and M. Newton, *Langmuir* 18, 2636 (2002).

7) H. Masoud and J. D. Felske, *Physics of Fluids* 21, 042102 (2009).

8) A. Petsi and V. Burganos, *Physical Review E* 78, 036324 (2008).

9) U. Thiele and E. Knobloch, *New Journal of Physics* 8, 313 (2006).

10) J. K. Park, J. Ryu, B. C. Koo, S. Lee, and K. H. Kang, *Soft Matter* 8, 11889 (2012).

11) R. Bhardwaj, X. Fang, and D. Attinger, *New Journal of Physics* 11, 075020 (2009).

12) D. Orejon, K. Sefiane, and M. E. Shanahan, *Langmuir* 27, 12834 (2011).

13) K. H. Kang, S. J. Lee, C. M. Lee, and I. S. Kang, *Measurement Science and Technology* 15, 1104 (2004).

14) T. K. Pradhan and P. K. Panigrahi, *Experiments in Fluids* 56, 1 (2015).

15) H. Kim, S. Große, G. E. Elsinga, and J. Westerweel, *Experiments in Fluids* 51, 395 (2011).

16) J. A. Howarter and J. P. Youngblood, *Langmuir* 22, 11142 (2006).

17) J. A. Howarter and J. P. Youngblood, *Macromolecules* 40, 1128 (2007).

18) D. K. Schwartz, *Annual Review of Physical Chemistry* 52, 107 (2001).

19) X. Zhao and R. Kopelman, *The Journal of Physical Chemistry* 100, 11014 (1996).

20) K.-I. Iimura, Y. Nakajima, and T. Kato, Thin *Solid Films* 379, 230 (2000).
21) A. Fellah, N. Belmiloud, R. G. Haverkamp, Y. Hemar, D. Otter, and M. A. Williams, *Carbohydrate Polymers* 87, 806 (2012).
22) R. J. Adrian and J. Westerweel, *Particle image velocimetry*, Cambridge University Press, (2010).
23) B. Wieneke, *Experiments in Fluids* 45, 549 (2008).
24) N. Shahidzadeh-Bonn, S. Rafai, A. Azouni, and D. Bonn, *Journal of Fluid Mechanics* 549, 307 (2006).
25) B. Weon, J. Je, and C. Poulard, *AIP Advances* 1, 012102(2011).
26) E. Detrich, W. Sander, W. V. Claas, H. Kevin, K. E. Stefan, J. W. Z. Harold, and L. Detlef, *Journal of Fluid Mechanics* 794, 45-67 (2016).
27) W. Den, H. Bai, and Y. Kang, *Journal of The Electro-chemical Society* 153, G149 (2006).
28) H. Hu and R. G. Larson, *The Journal of Physical Chemistry B* 110, 7090 (2006).
29) G. E. Elsinga, *TUDelft PhD thesis* (2008).
30) D. Mampallil, D. van den Ende, and F. Mugele, *Applied Physics Letters* 99, 154102 (2011).
31) H. Lee, S. Yun, S. H. Ko, and K. H. Kang, *Biomicrofluidics* 3, 044113 (2009).
32) H. Hu and R. G. Larson, *Langmuir* 21, 3963 (2005).